Lattice Boltzmann Solution of the Lid-Driven Cavity Problem

Rithwik Shankar Raj

1 Introduction

The lid-driven cavity problem is a standard benchmark for incompressible computational fluid dynamics because it combines a simple square geometry with nontrivial recirculating flow physics. A constant tangential velocity is imposed at the top wall, while the remaining walls are stationary and no-slip. The resulting motion generates a primary vortex inside the cavity and, as the Reynolds number increases, sharper shear layers and secondary recirculation regions near the corners.

In the present work, the flow is solved using the Lattice Boltzmann Method. Unlike traditional Navier–Stokes solvers, LBM uses a mesoscopic kinetic formulation in which particle distribution functions evolve on a discrete lattice.

2 Problem Definition

A square cavity of side length $L = H = 1$ is considered. The top lid moves with constant horizontal velocity U_{lid}, while the left, right, and bottom walls remain stationary. The Reynolds number is defined as

$$Re = \frac{U_{\text{lid}} L}{\nu}, \tag{1}$$

where ν is the kinematic viscosity.

The simulations reported here focus on

$$Re = 100, \qquad Re = 400, \qquad Re = 1000.$$

For LBM, the Reynolds number is commonly expressed in lattice units as

$$Re = \frac{U_0 N}{\nu}, \tag{2}$$

where U_0 is the lid velocity in lattice units and N is the characteristic grid size.

Table 1: General simulation parameters for the lid-driven cavity problem.

Quantity	Value
Cavity length, L	1
Cavity height, H	1
Reynolds numbers considered	$100,\ 400,\ 1000$
Lattice model	D2Q9
Collision model	BGK / single-relaxation-time
Fine grid used for main solutions	$N_x = N_y = 400$
Grids used for convergence study	$N = 50,\ 100,\ 200$
Finest reference grid for error study	$N = 400$
Tolerance for $Re = 100$ and $Re = 400$	10^{-11}
Tolerance for $Re = 1000$	5×10^{-7}

3 Lattice Boltzmann Formulation

3.1 Algorithm overview

The simulation procedure is as follows:

1. Define the computational domain and the input parameters.
2. Initialize the particle distribution functions.
3. Compute the LBM update:
   (a) evaluate the equilibrium distribution function,
   (b) perform the collision step,
   (c) perform the streaming step,
   (d) apply boundary conditions,
   (e) recover macroscopic variables such as density and velocity.
4. Repeat until the convergence criterion is satisfied.
5. Output the data for post-processing.

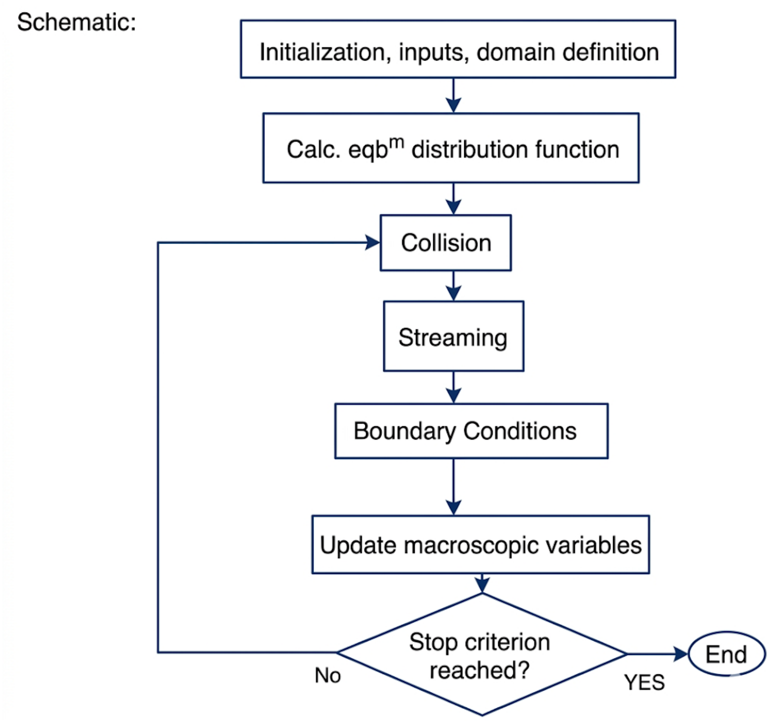

Figure 1: Schematic of the Lattice Boltzmann solution procedure.

3.2 Domain and lattice arrangement

The physical domain is a square lid-driven cavity. A D2Q9 lattice is used, meaning that each lattice node supports nine discrete particle velocities: one rest particle, four axial directions, and four diagonal directions.

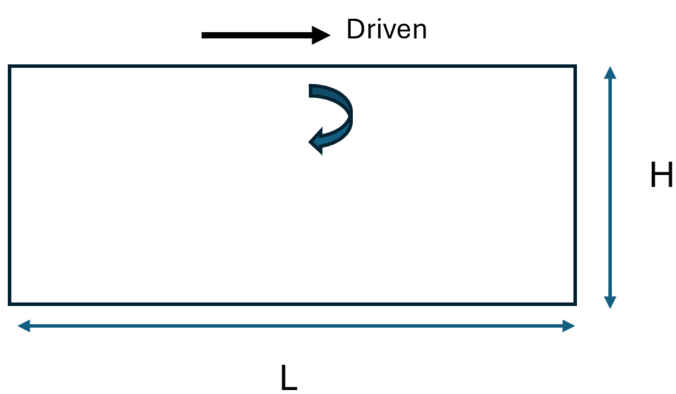

Figure 2: Schematic of the lid-driven cavity domain.

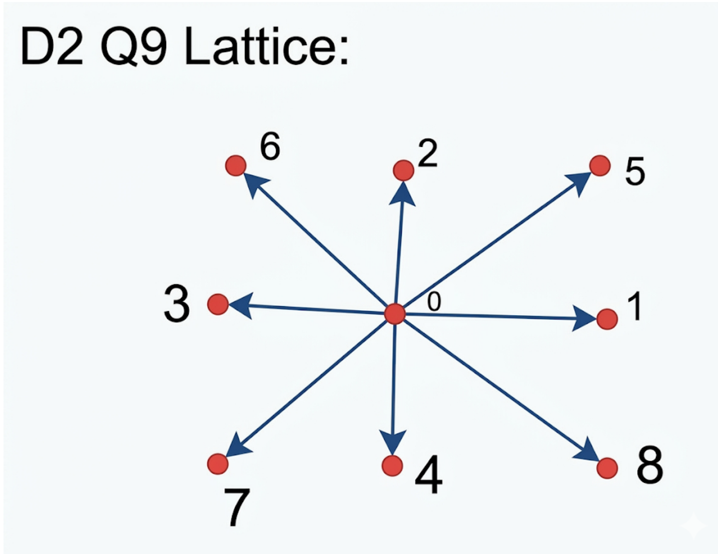

Figure 3: D2Q9 lattice showing the discrete velocity directions.

3.3 D2Q9 discrete velocities and weights

For the D2Q9 model, the discrete lattice velocities are

$$\boldsymbol{c}_0 = (0,0), \tag{3}$$

$$\boldsymbol{c}_1 = (1,0), \qquad \boldsymbol{c}_2 = (0,1), \qquad \boldsymbol{c}_3 = (-1,0), \qquad \boldsymbol{c}_4 = (0,-1), \tag{4}$$

$$\boldsymbol{c}_5 = (1,1), \qquad \boldsymbol{c}_6 = (-1,1), \qquad \boldsymbol{c}_7 = (-1,-1), \qquad \boldsymbol{c}_8 = (1,-1). \tag{5}$$

The corresponding weights are

$$w_0 = \frac{4}{9}, \qquad w_{1,2,3,4} = \frac{1}{9}, \qquad w_{5,6,7,8} = \frac{1}{36}, \tag{6}$$

with

$$\sum_{i=0}^{8} w_i = 1. \tag{7}$$

3.4 BGK evolution equation

The discrete Boltzmann transport equation with the BGK collision model is written as

$$f_i(\boldsymbol{x} + \boldsymbol{c}_i \Delta t,\, t + \Delta t) - f_i(\boldsymbol{x}, t) = -\frac{1}{\tau}\left[f_i(\boldsymbol{x}, t) - f_i^{\mathrm{eq}}(\boldsymbol{x}, t)\right], \tag{8}$$

where f_i is the particle distribution function in direction i, f_i^{eq} is the corresponding equilibrium distribution, and τ is the relaxation time.

The collision step may be written separately as

$$f_i^*(\boldsymbol{x}, t) = f_i(\boldsymbol{x}, t) - \omega \left[f_i(\boldsymbol{x}, t) - f_i^{\mathrm{eq}}(\boldsymbol{x}, t) \right], \qquad \omega = \frac{1}{\tau}, \tag{9}$$

followed by the streaming step

$$f_i(\boldsymbol{x} + \boldsymbol{c}_i \Delta t,\, t + \Delta t) = f_i^*(\boldsymbol{x}, t). \tag{10}$$

3.5 Equilibrium distribution function

For low-Mach-number incompressible flow, the equilibrium distribution function is

$$f_i^{\mathrm{eq}} = w_i \rho \left[1 + 3(\boldsymbol{c}_i \cdot \boldsymbol{u}) + \frac{9}{2}(\boldsymbol{c}_i \cdot \boldsymbol{u})^2 - \frac{3}{2}(\boldsymbol{u} \cdot \boldsymbol{u}) \right], \tag{11}$$

where ρ is the density and $\boldsymbol{u} = (u, v)$ is the macroscopic velocity.

3.6 Macroscopic variables

The density and momentum are obtained from the distribution functions through

$$\rho = \sum_{i=0}^{8} f_i, \tag{12}$$

$$\rho \boldsymbol{u} = \sum_{i=0}^{8} \boldsymbol{c}_i f_i. \tag{13}$$

Thus the velocity components are

$$u = \frac{1}{\rho} \sum_{i=0}^{8} c_{ix} f_i, \qquad v = \frac{1}{\rho} \sum_{i=0}^{8} c_{iy} f_i. \tag{14}$$

3.7 Relaxation time and viscosity

The kinematic viscosity is related to the relaxation time through

$$\nu = c_s^2 \left(\tau - \frac{1}{2} \right), \tag{15}$$

where the lattice speed of sound is

$$c_s = \frac{1}{\sqrt{3}}. \tag{16}$$

Since $c_s^2 = 1/3$ in lattice units, Eq. (15) may also be written as

$$\nu = \frac{1}{3} \left(\tau - \frac{1}{2} \right) \qquad \Longrightarrow \qquad \tau = 3\nu + \frac{1}{2}. \tag{17}$$

For the fine-grid examples,

$$\text{Case 1:} \quad N_x = N_y = 400, \quad U_0 = 0.01, \quad \nu = 0.04, \quad \tau = 3\nu + 0.5 = 0.62, \quad Re = \frac{U_0 N}{\nu} = 100, \tag{18}$$

$$\text{Case 2:} \quad N_x = N_y = 400, \quad U_0 = 0.04, \quad \nu = 0.04, \quad \tau = 0.62, \quad Re = \frac{U_0 N}{\nu} = 400. \tag{19}$$

3.8 Boundary conditions

Stationary walls at the left, right, and bottom boundaries are implemented with standard bounce-back boundary conditions. In schematic form, the outgoing populations are reflected back into the fluid:

$$\text{Left wall:} \qquad f_1 = f_3, \qquad f_5 = f_7, \qquad f_8 = f_6, \tag{20}$$

$$\text{Right wall:} \qquad f_3 = f_1, \qquad f_6 = f_8, \qquad f_7 = f_5, \tag{21}$$

$$\text{Bottom wall:} \qquad f_2 = f_4, \qquad f_5 = f_7, \qquad f_6 = f_8. \tag{22}$$

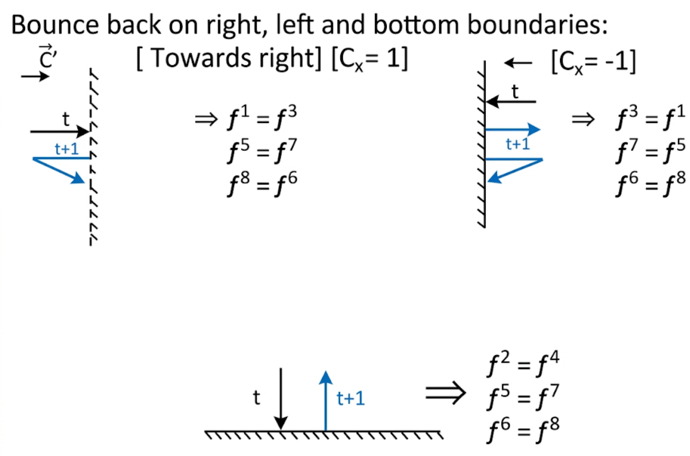

Figure 4: Bounce-back treatment at the stationary left, right, and bottom walls.

For the moving top lid, a velocity boundary treatment is used. The density near the top wall is written as

$$\rho_t = f_0 + f_1 + f_3 + 2\left(f_2 + f_5 + f_6\right), \tag{23}$$

and the unknown incoming distributions at the lid are updated as

$$f_4 = f_2, \qquad f_8 = f_6 + \frac{\rho_t U_0}{6}, \qquad f_7 = f_5 - \frac{\rho_t U_0}{6}. \tag{24}$$

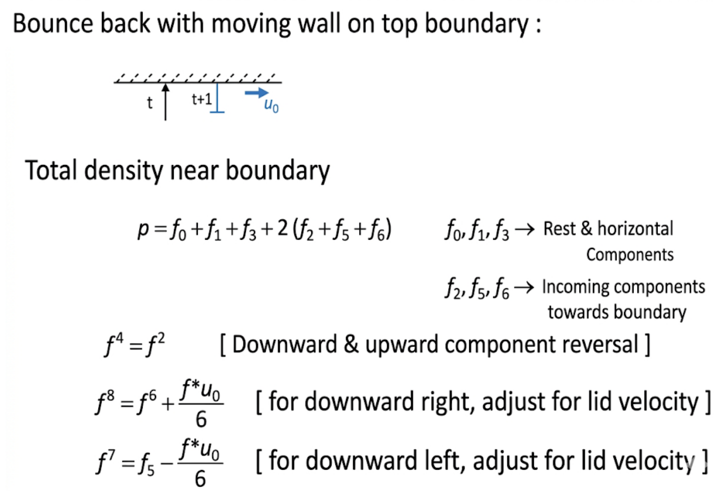

Figure 5: Moving-wall boundary treatment at the top lid.

3.9 Convergence criterion

The steady-state solution is identified through the L_2 norm of the change in the horizontal and vertical velocity fields between successive iterations:

$$\mathcal{R}^{(n)} = \left[\sum_{i,j} \left(u_{i,j}^{(n+1)} - u_{i,j}^{(n)} \right)^2 + \sum_{i,j} \left(v_{i,j}^{(n+1)} - v_{i,j}^{(n)} \right)^2 \right]^{1/2} . \tag{25}$$

The simulation is advanced until $\mathcal{R}^{(n)}$ falls below the prescribed tolerance.

4 Results and Discussion

4.1 Case I: Reynolds number $Re = 100$

The Lattice Boltzmann method was first applied to the lid-driven cavity problem for $Re = 100$. At this Reynolds number the flow is primarily viscous and remains smooth and laminar throughout the cavity. The horizontal velocity is largest near the moving lid and gradually decreases toward the bottom wall. The vertical velocity field reflects the recirculating motion generated by the lid, with clear redirection of the fluid near the walls and corners.

A primary vortex forms near the center of the cavity. The flow is relatively symmetric, and the velocity contours vary smoothly, consistent with the dominance of viscous effects. Boundary layers are visible near the lid and side walls, where the gradients in the horizontal velocity are strongest.

The residual history shows monotonic decay toward a steady solution. The tolerance for this case was taken as 10^{-11}, and the fine-grid solution required a large number of iterations because of the explicit nature of the LBM update and the selected relaxation parameters.

To assess solution accuracy, the centerline horizontal velocity $u(y)$ and centerline vertical velocity

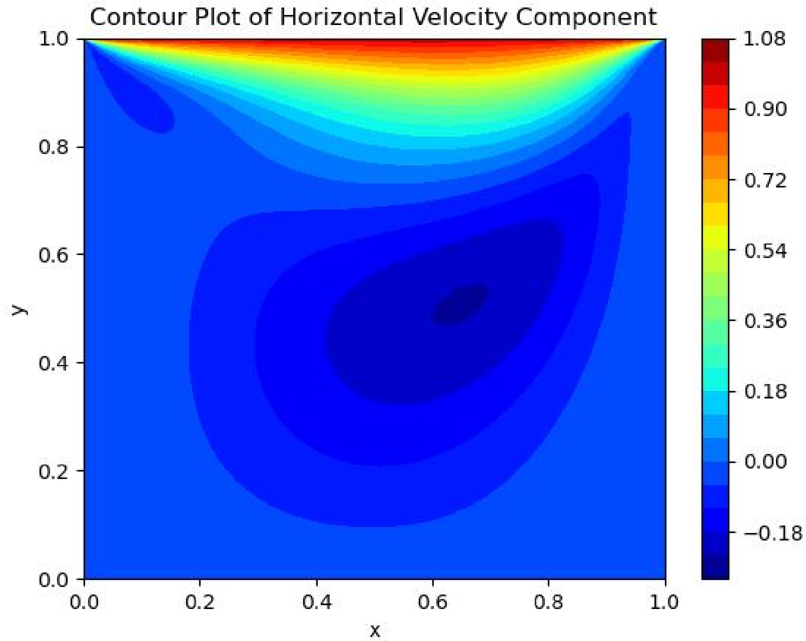

Figure 6: Plot of the horizontal velocity (u) for $Re = 100$.

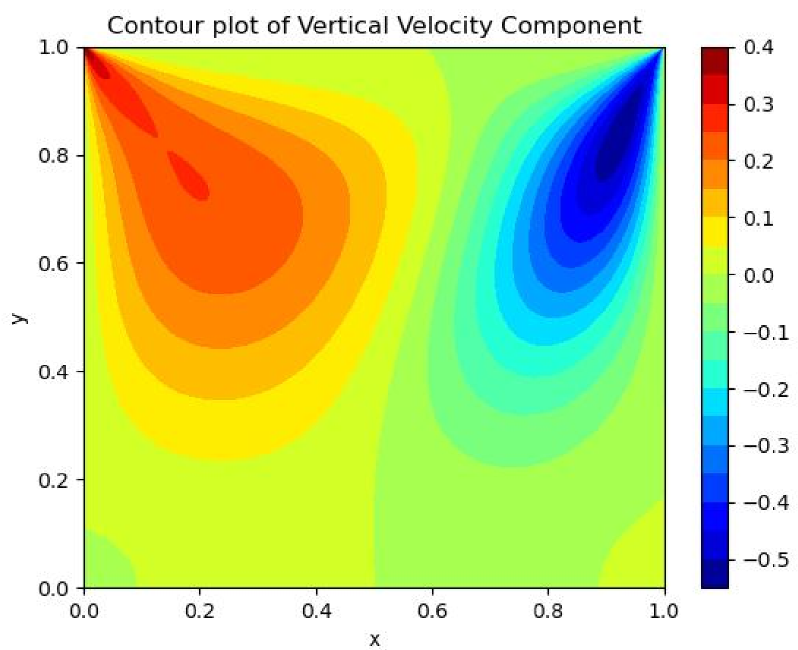

Figure 7: Plot of vertical component of velocity (v) for $Re = 100$.

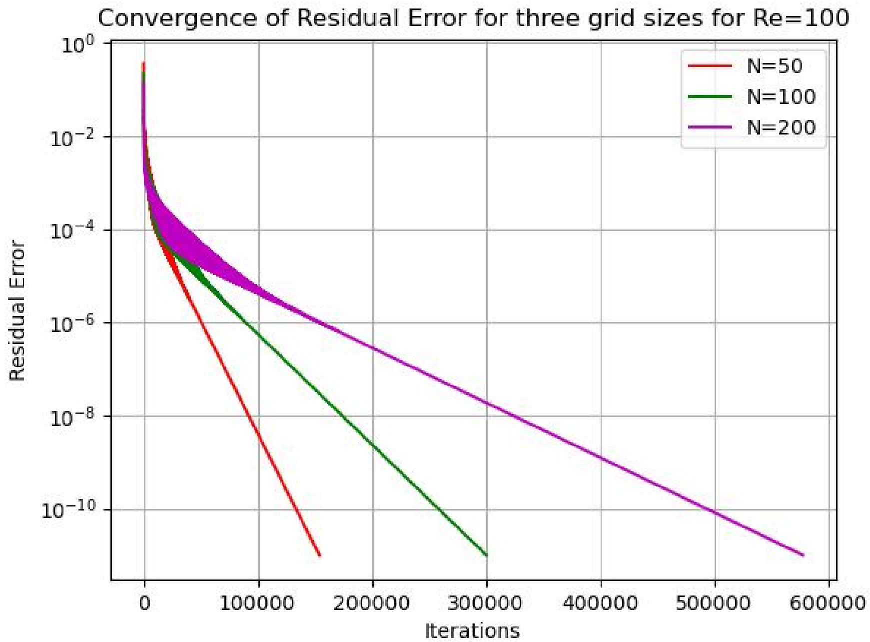

Figure 8: Plot of residual error with iterations for $Re = 100$.

$v(x)$ are compared with the benchmark data reported by Ghia et al. The numerical and benchmark profiles follow one another closely, indicating that the method accurately captures the principal recirculating structure of the cavity flow.

The reference values from Ghia et al. were tabulated and then interpolated before plotting in the original workflow.

The streamline plot of the net velocity field and the contour plot of the horizontal velocity confirm the presence of a dominant central vortex. The contour plot also shows the early development of recirculation near the lower corners.

4.2 Case II: Reynolds number $Re = 400$

The same method was then used for $Re = 400$. At this higher Reynolds number, inertial effects are stronger and the velocity field becomes more asymmetric. The main vortex remains the dominant feature of the flow, but sharper gradients appear near the moving lid and the corner regions.

Compared with the lower-Reynolds-number case, the contours are more distorted and the recirculating motion is more pronounced. The boundary layers near the top wall and the side walls are thinner, and shear effects become more visible in the vertical velocity field.

The residual still decreases toward the steady state, although stronger oscillations appear in the convergence history because of the increased inertial effects. The number of iterations required to achieve convergence is significantly larger than in the lower-Reynolds-number case.

The centerline velocity profiles are again compared against the benchmark solution. The numerical

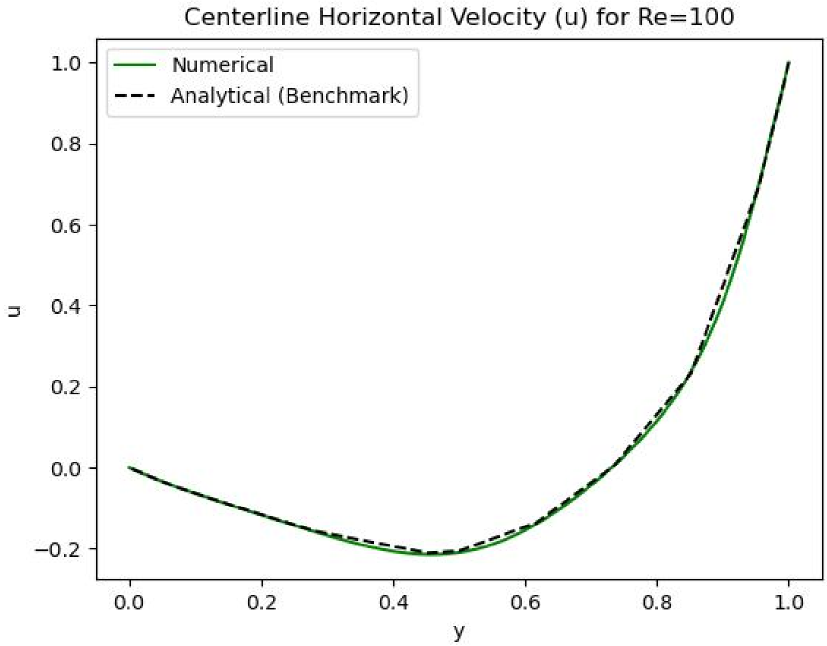

Figure 9: Centerline horizontal velocity (u) for $Re = 100$.

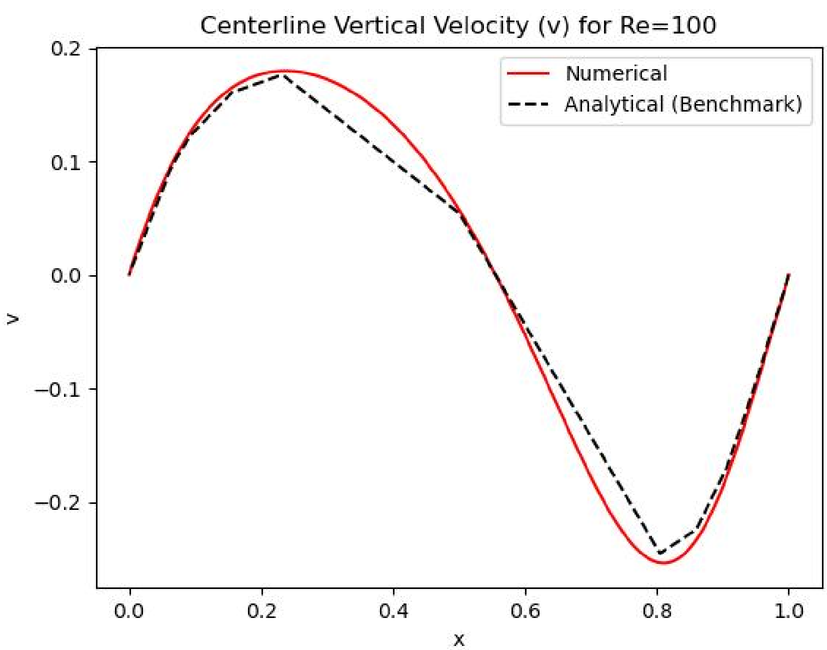

Figure 10: Centerline vertical velocity (v) for $Re = 100$.

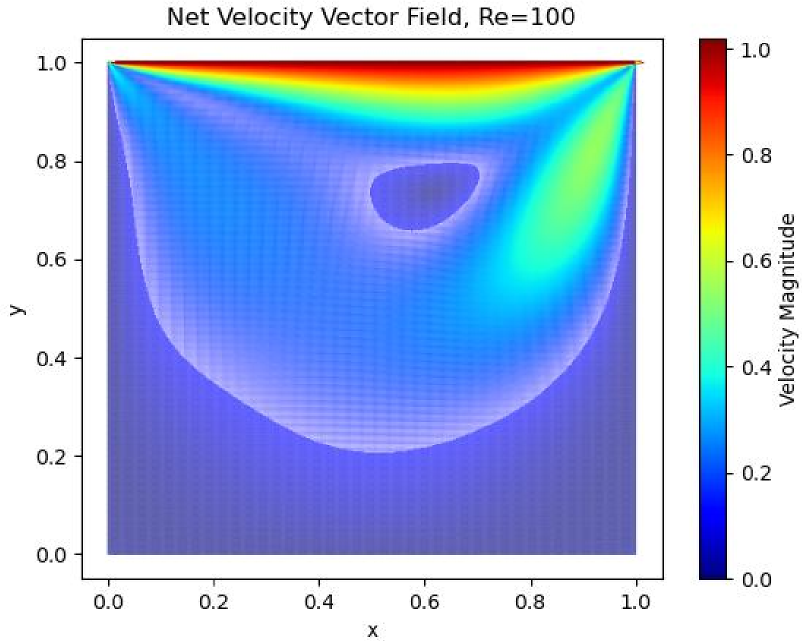

Figure 11: Streamline plot of net velocity vector for $Re = 100$.

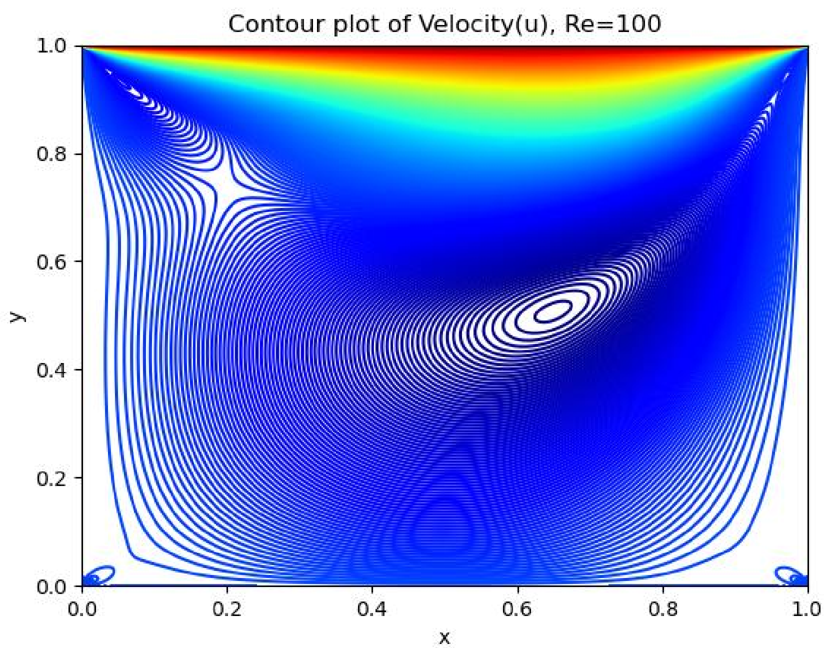

Figure 12: Contour plot of horizontal velocity (u) for $Re = 100$.

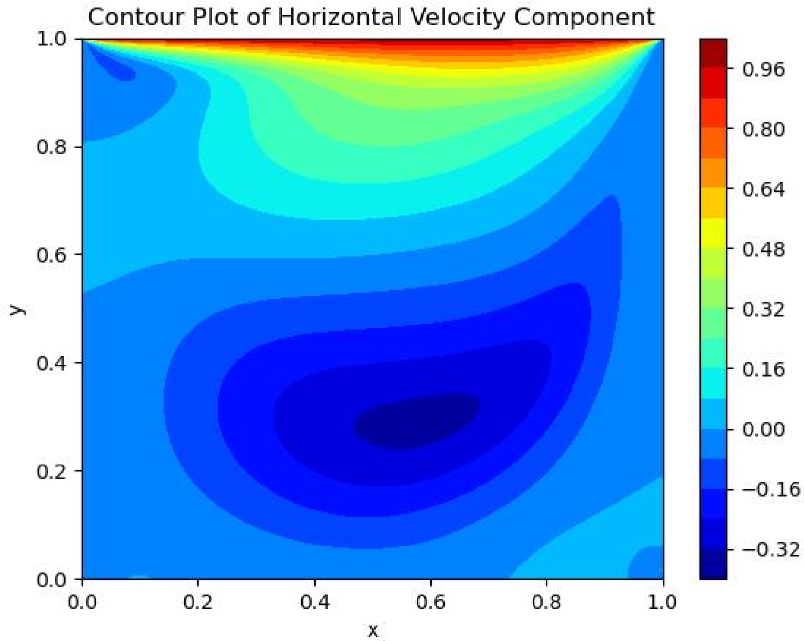

Figure 13: Plot of the horizontal velocity (u) for $Re = 400$.

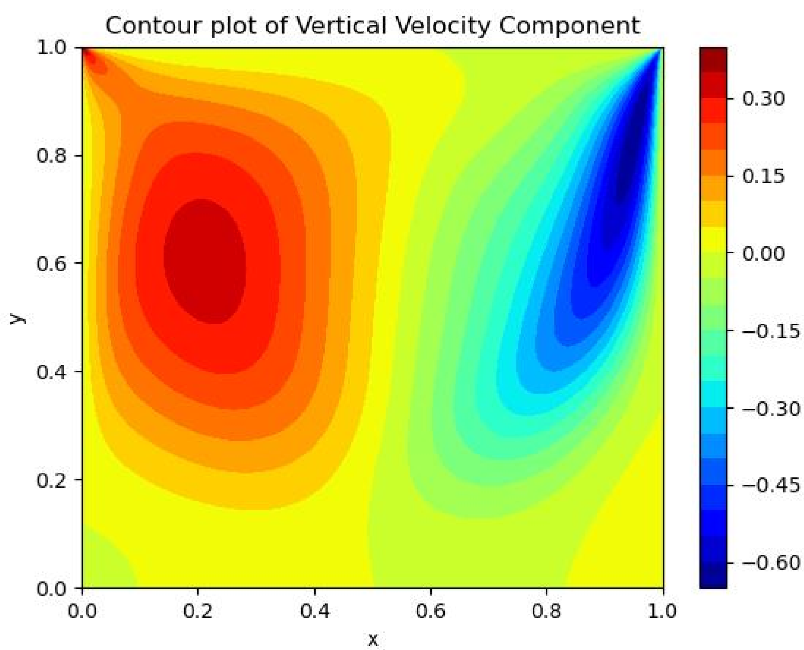

Figure 14: Plot of vertical component of velocity (v) for $Re = 400$.

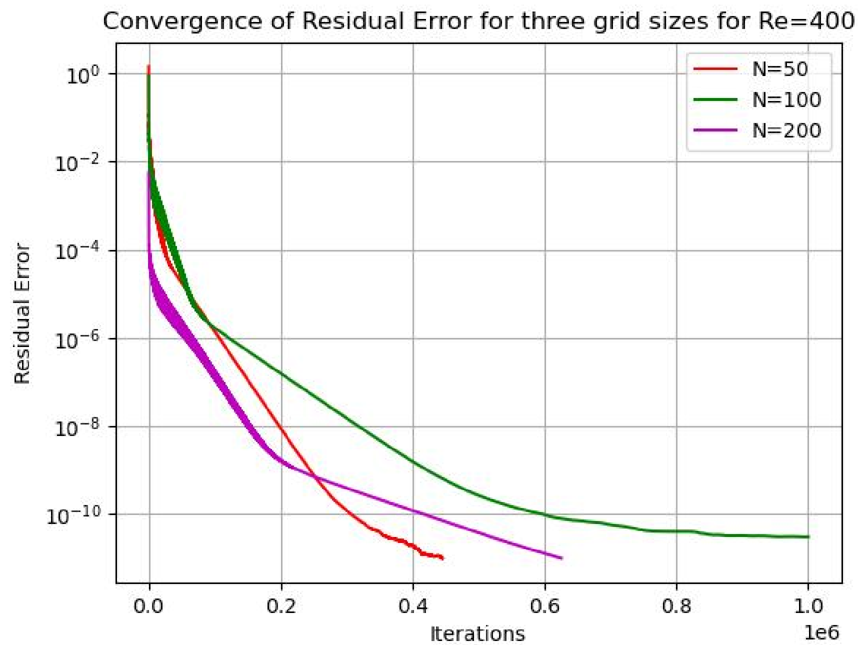

Figure 15: Plot of residual error with iterations for $Re = 400$.

curves closely follow the benchmark data and accurately reproduce the stronger gradients and more pronounced curvature associated with the higher Reynolds number.

The streamline and contour plots show that secondary recirculation is more prominent than in the $Re = 100$ case, especially in the corner regions of the cavity.

4.3 Case III: Reynolds number $Re = 1000$

A third set of simulations was carried out for $Re = 1000$. At this Reynolds number, inertial effects become even more dominant and the cavity flow develops stronger asymmetry, sharper shear layers, and more distinct corner vortices.

The main vortex is still centered within the cavity, but it is more distorted than in the lower-Reynolds-number cases. The contour structure shows stronger gradients, more pronounced boundary-layer effects, and clearer signs of secondary recirculation near the corners.

The convergence history for $Re = 1000$ remains stable overall, but it shows larger oscillations than the lower-Reynolds-number cases. This reflects the increased difficulty of maintaining stability as the Reynolds number rises and the effective viscosity decreases.

The centerline velocity profiles continue to follow the benchmark trends well, indicating that the LBM implementation remains accurate even as the flow becomes more complex.

The streamline plot and contour plot show that the secondary vortices and corner recirculation zones are considerably more prominent at $Re = 1000$ than in the $Re = 100$ and $Re = 400$ cases.

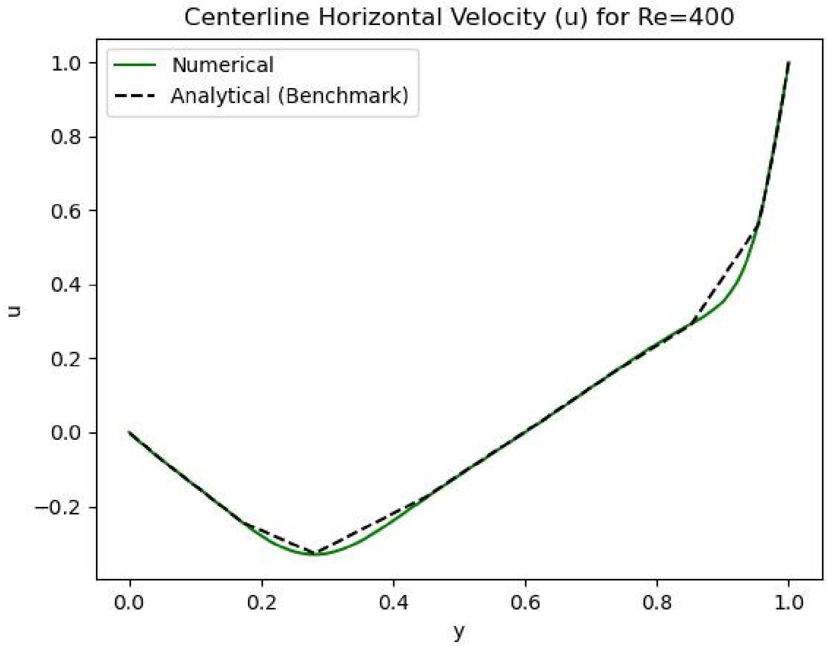

Figure 16: Centerline horizontal velocity (u) for $Re = 400$.

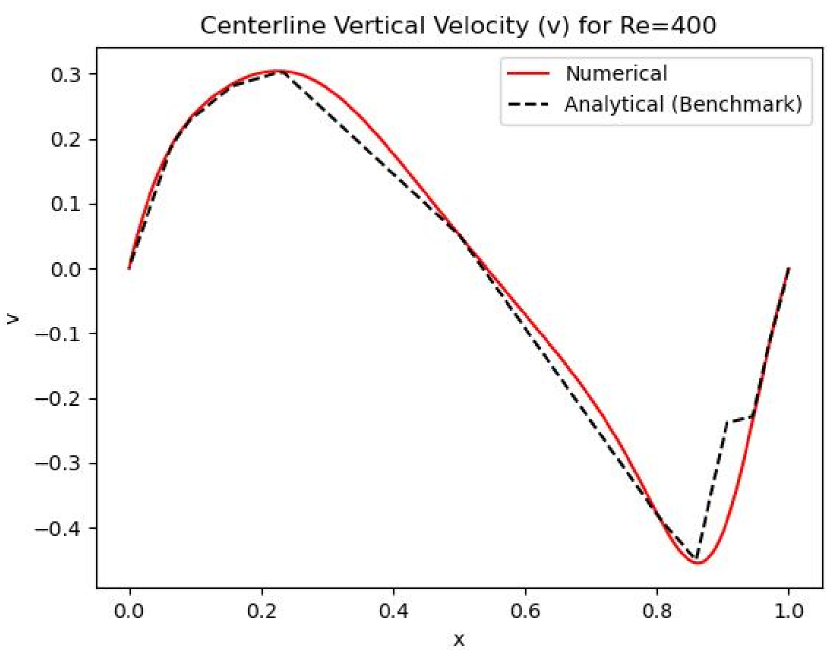

Figure 17: Centerline vertical velocity (v) for $Re = 400$.

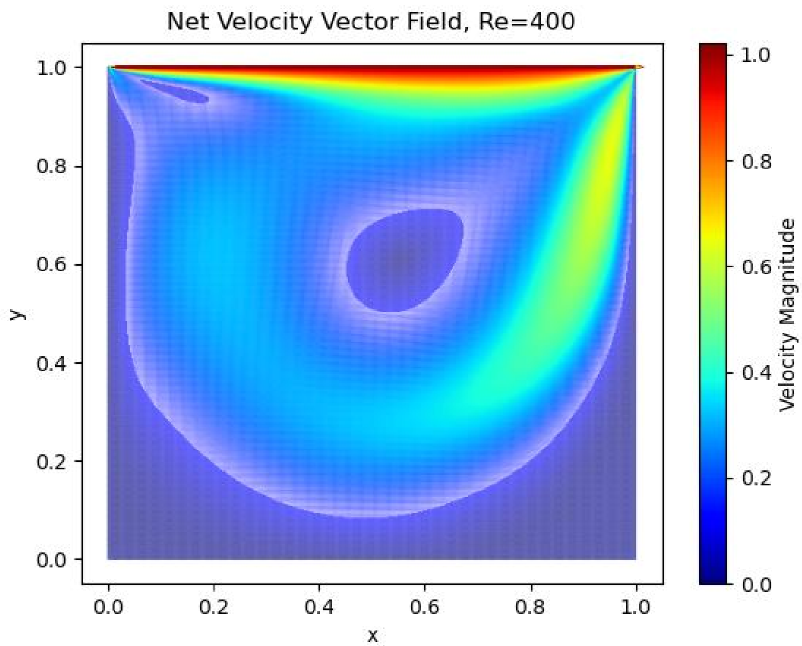

Figure 18: Streamline plot of net velocity vector for $Re = 400$.

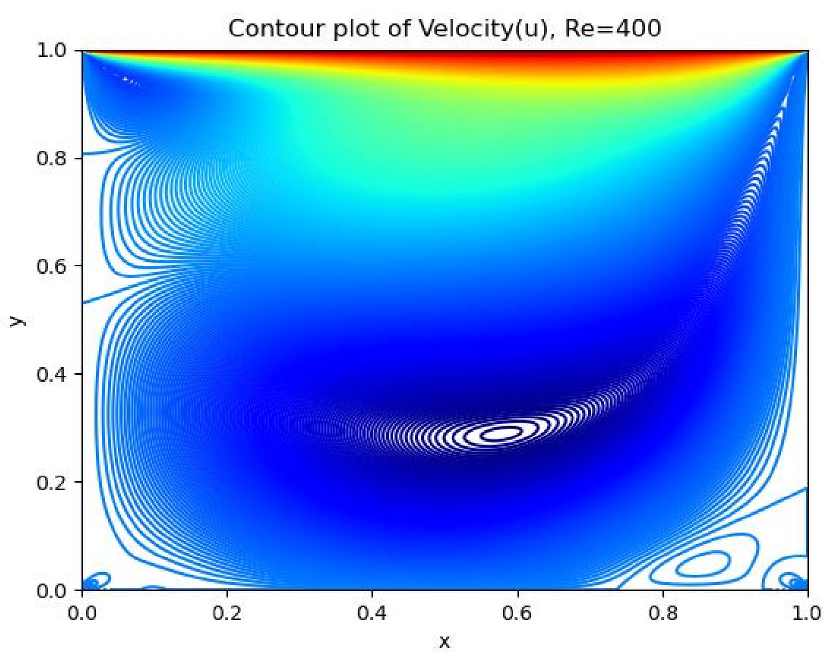

Figure 19: Contour plot of horizontal velocity (u) for $Re = 400$.

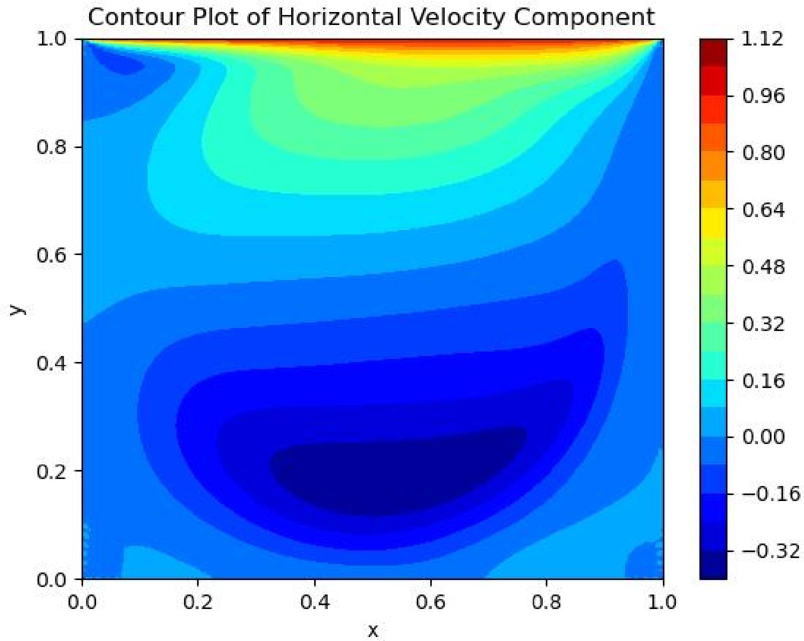

Figure 20: Plot of the horizontal velocity (u) for $Re = 1000$.

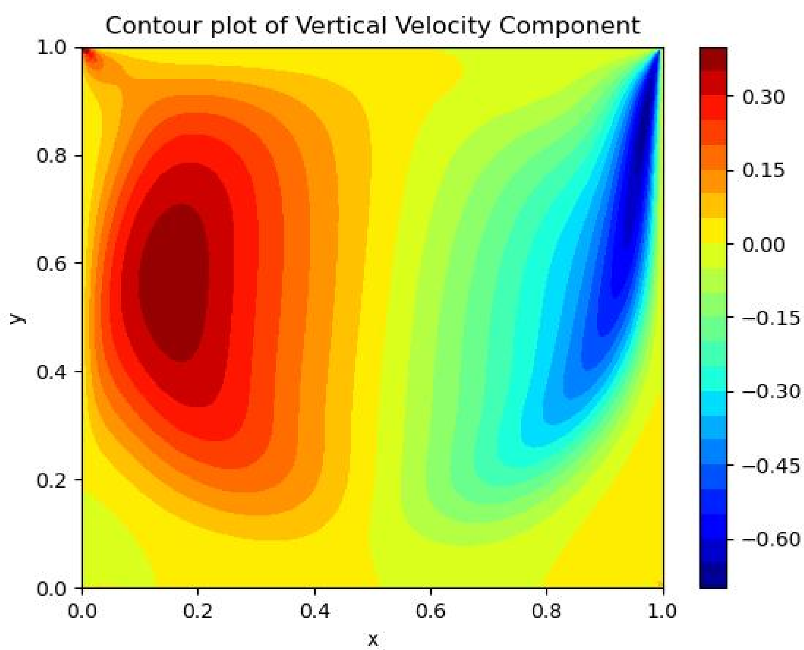

Figure 21: Plot of vertical component of velocity (v) for $Re = 1000$.

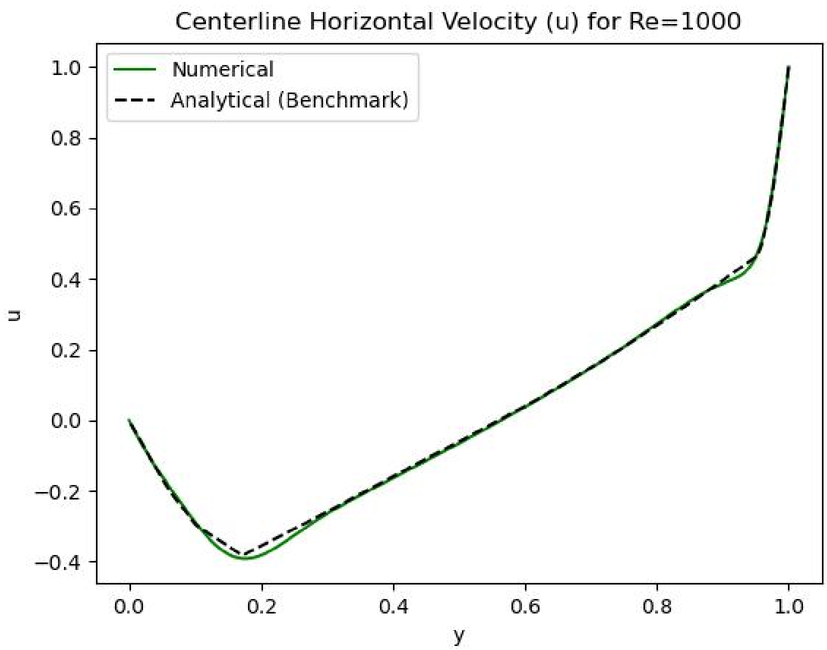

Figure 22: Centerline horizontal velocity (u) for $Re = 1000$.

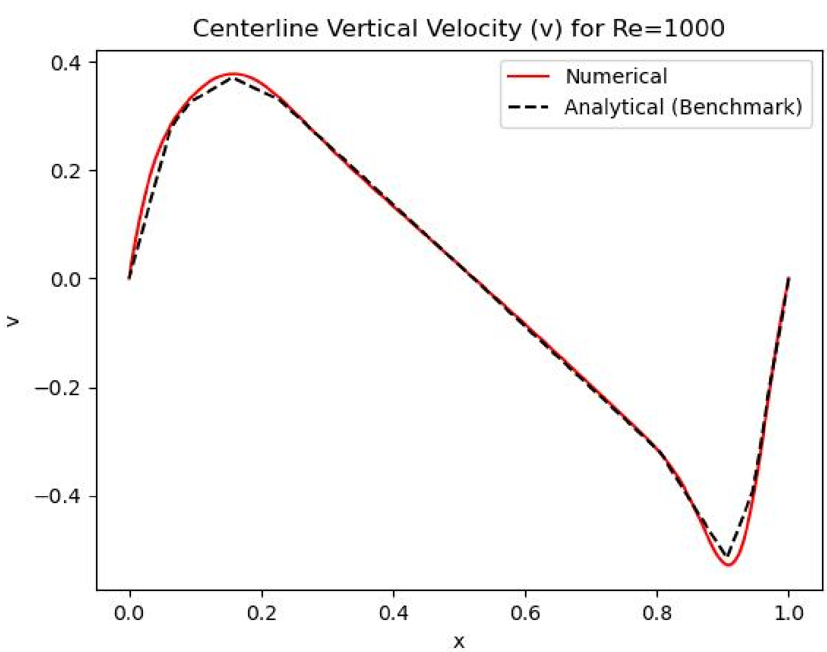

Figure 23: Centerline vertical velocity (v) for $Re = 1000$.

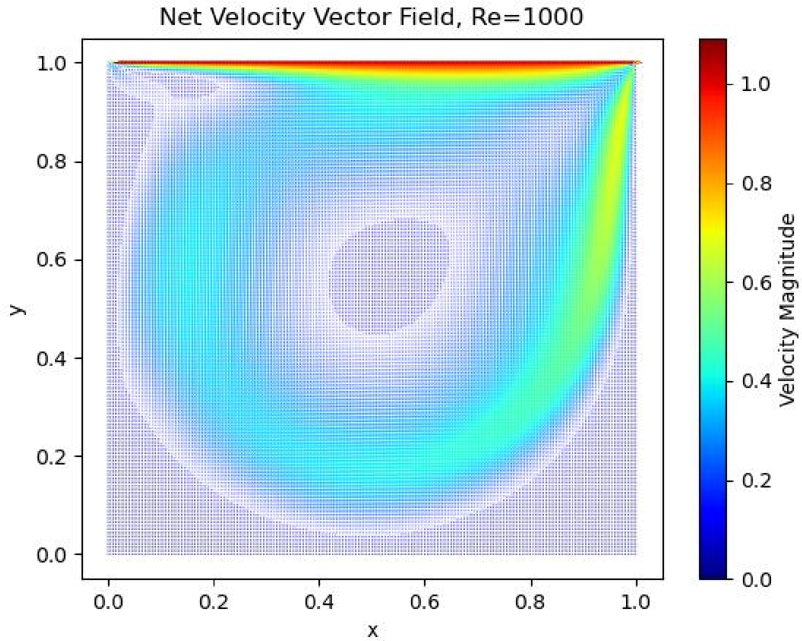

Figure 24: Streamline plot of net velocity vector for $Re = 1000$.

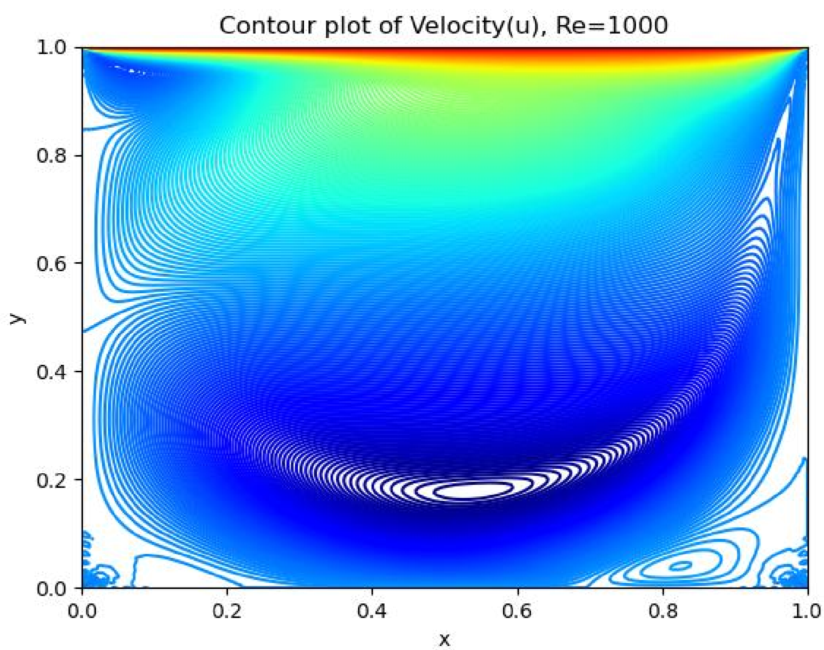

Figure 25: Contour plot of horizontal velocity (u) for $Re = 1000$.

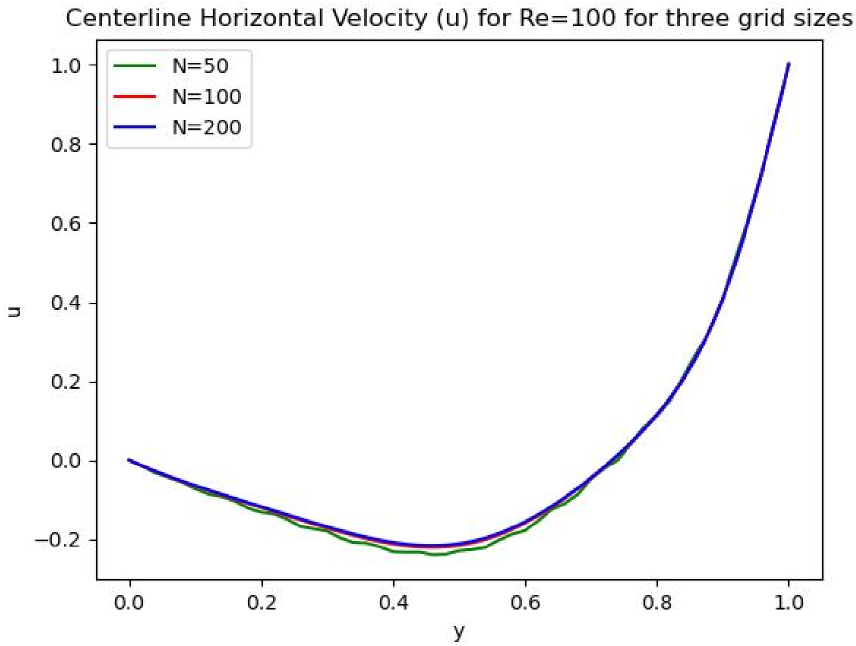

Figure 26: Centerline horizontal velocity for three grid sizes ($N = 50,\ 100,\ 200$) for $Re = 100$.

5 Grid-Convergence Assessment

To validate the numerical solution, the centerline velocity profiles were computed on three different grid resolutions,

$$N = 50, \qquad 100, \qquad 200,$$

with the grid spacing halved at each refinement step.

For $Re = 100$, the centerline horizontal and vertical velocity profiles move progressively closer to the benchmark values as the grid is refined. This indicates that the numerical scheme increasingly captures the boundary-layer structure and the main recirculating vortex with improved fidelity.

For $Re = 400$, the same trend is observed. The horizontal centerline velocity aligns more closely with the benchmark in the primary-vortex region as the grid is refined, while the vertical velocity profile more accurately captures the stronger gradients and vortex symmetry of the flow.

6 Effect of Relaxation Time and Mach Number

6.1 Relaxation time

The relaxation time is directly related to the kinematic viscosity through Eq. (15). For stability, the BGK LBM requires

$$\tau > \frac{1}{2}. \tag{26}$$

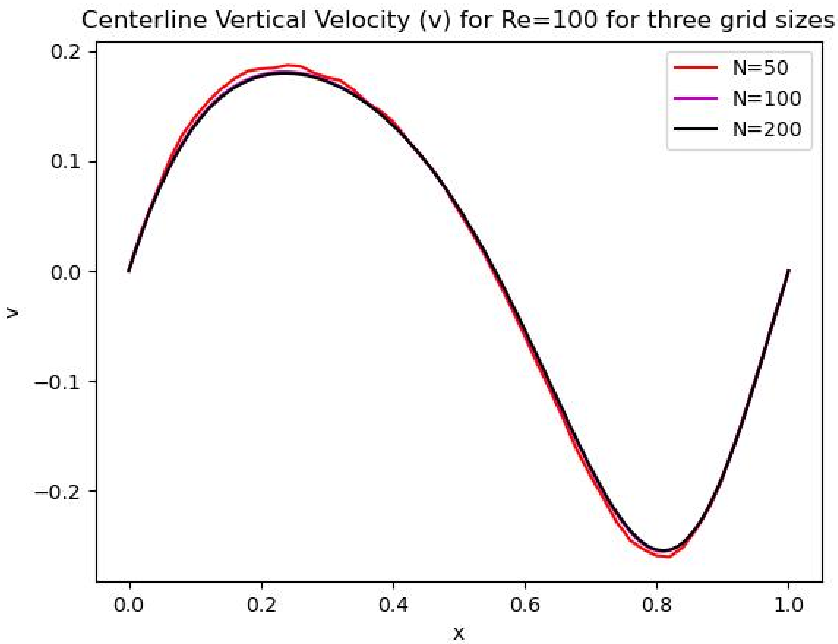

Figure 27: Centerline vertical velocity for three grid sizes ($N = 50,\ 100,\ 200$) for $Re = 100$.

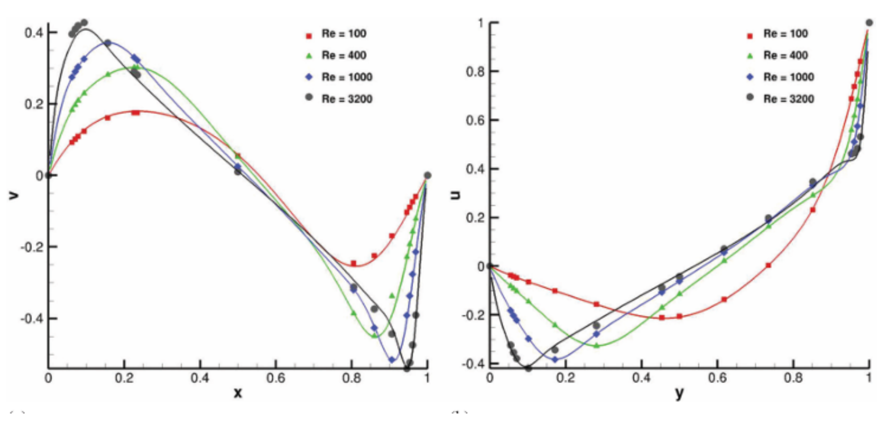

Figure 28: Centerline velocities for the lid-driven cavity: (a) vertical velocity variation and (b) horizontal velocity variation, results from Ghia et al. (1982).

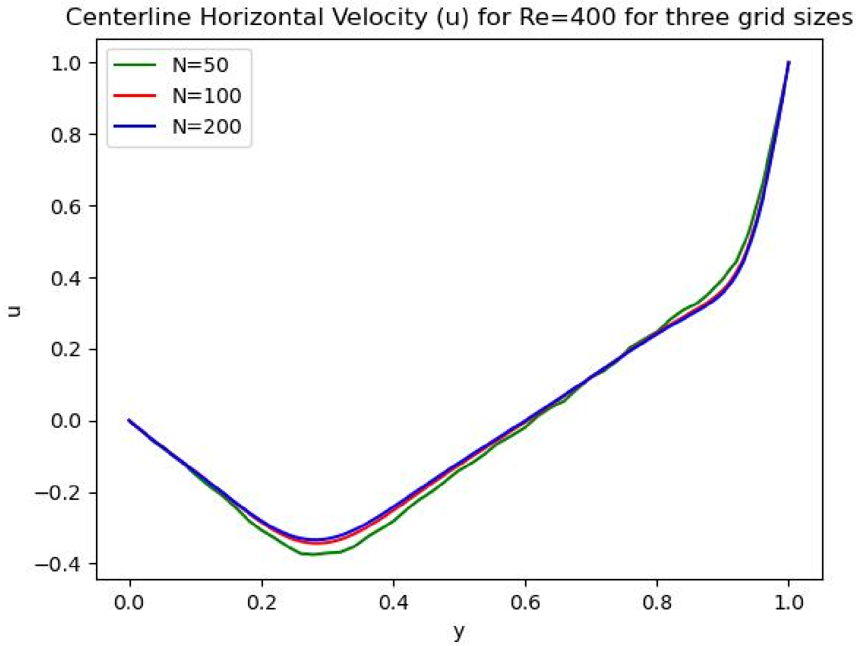

Figure 29: Centerline horizontal velocity for three grid sizes ($N = 50,\ 100,\ 200$) for $Re = 400$.

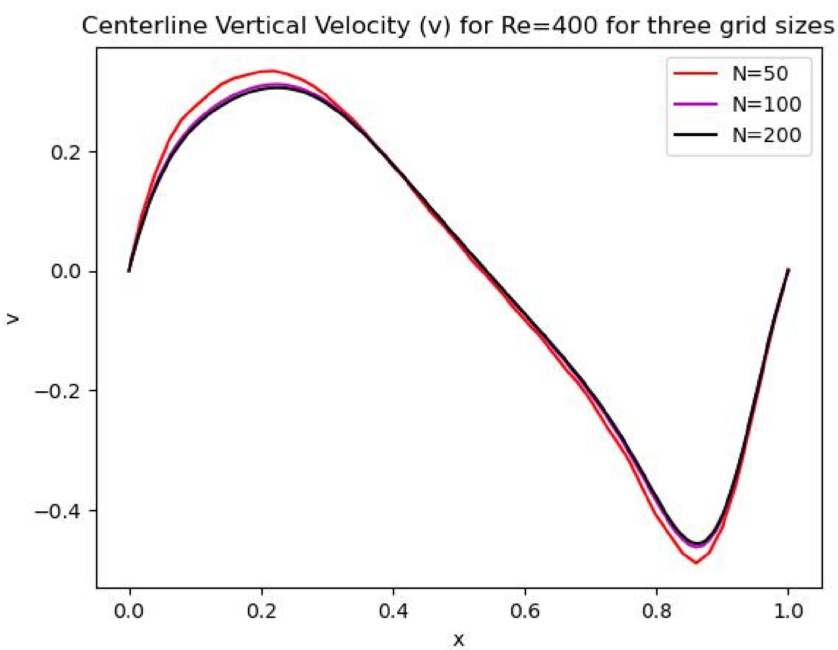

Figure 30: Centerline vertical velocity for three grid sizes ($N = 50,\ 100,\ 200$) for $Re = 400$.

As $\tau \to 0.5$, the viscosity becomes very small and the simulation becomes increasingly susceptible to numerical instability. On the other hand, larger values of τ increase dissipation and may reduce solution accuracy.

To study this effect, simulations were run for different values of τ while holding the Reynolds number fixed at $Re = 100$ through an appropriate choice of velocity, grid size, and viscosity. The residual histories show that convergence generally becomes faster as τ moves away from the lower stability limit, although excessively large values can degrade agreement with benchmark data.

6.2 Mach number

The Mach number is defined as

$$Ma = \frac{U}{c_s}. \tag{27}$$

For LBM to remain a good approximation to incompressible flow, the Mach number must remain small. Higher values of Ma introduce compressibility effects and can lead to instability.

Because $Re \propto U/\nu$, increasing the Reynolds number at fixed resolution often requires increasing the characteristic velocity, which in turn raises the Mach number. This restricts the range of feasible high-Reynolds-number simulations for a given grid.

To study this effect, the flow velocity U_0 was varied and the corresponding residual histories were examined. The results show that as U_0 increases, the number of iterations required for convergence increases and the oscillations in the residual become more pronounced. For sufficiently large velocities, the solution becomes unstable and the error grows rapidly.

7 Comparison with the Artificial Compressibility and Projection Methods

7.1 Artificial compressibility method

The artificial compressibility method introduces a pseudo-time derivative into the continuity equation so that the incompressibility constraint is recovered when the pseudo-time evolution reaches steady state. This makes the method naturally suited to steady-state problems. However, because the pseudo-time is not the real physical time, the method is not ideal for transient problems where the true time evolution of the pressure and velocity fields is important.

From a computational standpoint, the artificial compressibility method can be attractive for steady problems because it avoids solving a pressure Poisson equation at every iteration. However, it may require many pseudo-time iterations, and its stability is affected by additional timestep restrictions.

7.2 Projection method

The projection method enforces incompressibility at each physical timestep by first computing an intermediate velocity field and then solving a pressure Poisson equation to project that field onto a

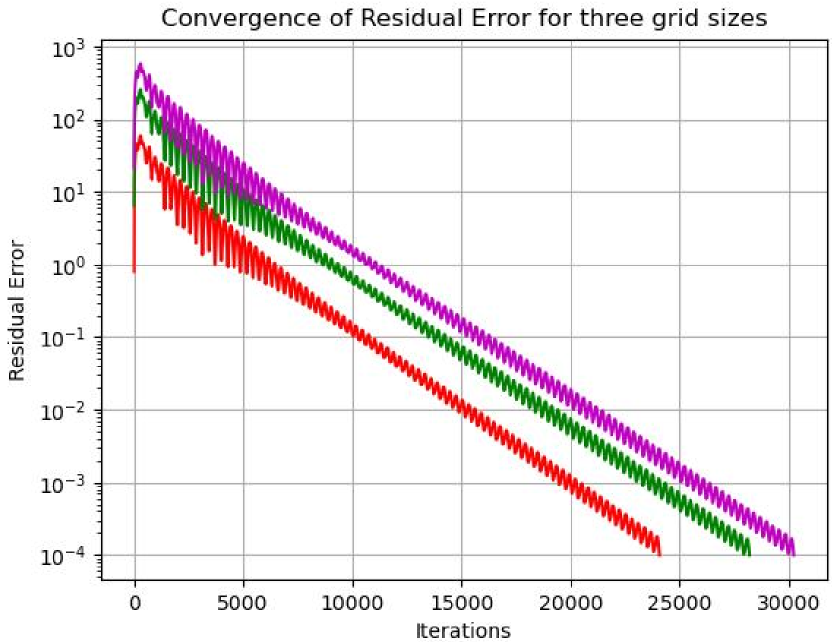

Figure 31: Convergence for $Re = 100$ for Artificial Compressibility.

divergence-free space. Because incompressibility is enforced at every timestep in physical time, the method is well suited to transient incompressible flows.

The main computational cost of the projection method comes from the repeated solution of the pressure Poisson equation. Nevertheless, the method provides strong pressure–velocity coupling and robust transient behavior.

7.3 Lattice Boltzmann method

The Lattice Boltzmann Method differs from both approaches in that it advances particle distribution functions directly through collision and streaming steps. The method is explicit in time, naturally suited to transient problems, and highly amenable to parallel implementation. At the same time, its stability and accuracy are sensitive to the relaxation time and Mach number, and sufficiently fine grids are required for high-Reynolds-number flows.

Overall, the projection method offers strong physical consistency for transient incompressible flow, the artificial compressibility method remains conceptually simple for steady-state problems, and the LBM provides a flexible and highly parallelizable mesoscopic alternative that performs very well for both steady and transient low-Mach-number flows.

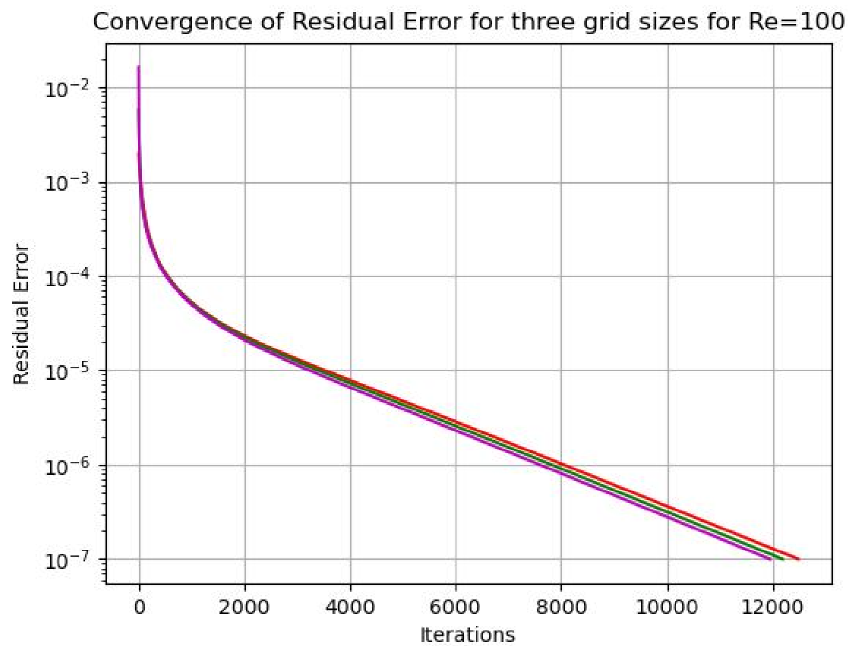

Figure 32: Convergence for $Re = 100$ for the Projection Method.

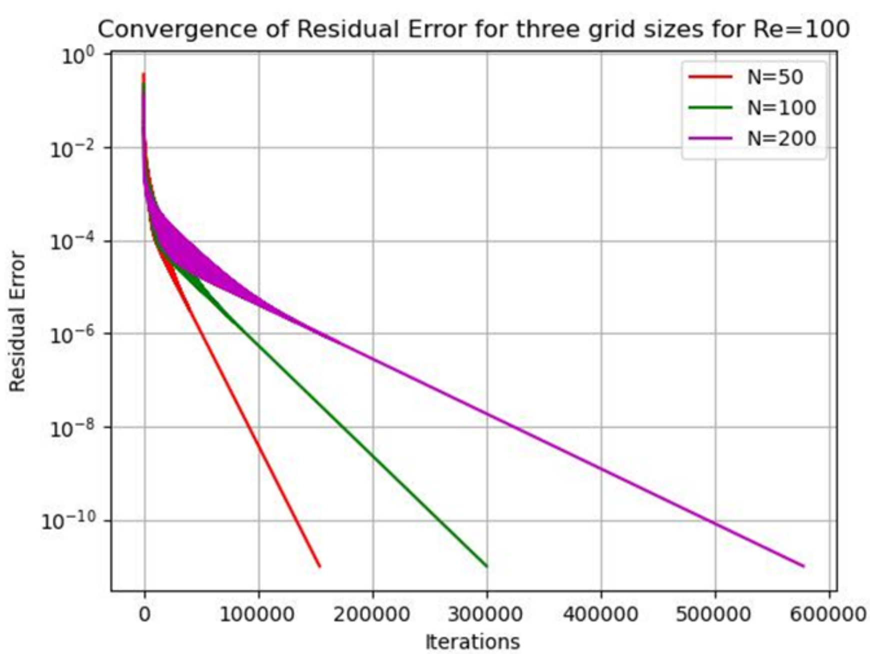

Figure 33: Convergence for $Re = 100$ for the Lattice Boltzmann Method.

8 Conclusions

A D2Q9 Lattice Boltzmann solver with the BGK collision model was used to simulate lid-driven cavity flow for Reynolds numbers $Re = 100$, $Re = 400$, and $Re = 1000$. The numerical results successfully reproduced the main features of cavity flow for all three Reynolds numbers, including the central recirculating vortex, the increasing asymmetry of the velocity field with increasing Reynolds number, and the growth of corner recirculation regions. The centerline velocity comparisons showed good agreement with the benchmark data of Ghia et al.

The grid-convergence and spatial-convergence studies demonstrated that the solution improves systematically with mesh refinement and that the spatial accuracy is close to second order. Additional studies on relaxation time and Mach number showed that the stability and convergence behavior of the LBM are strongly influenced by these parameters. In particular, the method becomes increasingly sensitive as τ approaches 0.5 or as the Mach number becomes too large.

Overall, the Lattice Boltzmann Method provides an accurate and flexible approach for incompressible lid-driven cavity flow, while also offering important advantages in simplicity of algorithmic structure and potential for parallel implementation.

References

[1] P. L. Bhatnagar, E. P. Gross, and M. Krook, "A model for collision processes in gases. I. Small amplitude processes in charged and neutral one-component systems," *Physical Review*, vol. 94, no. 3, pp. 511–525, 1954.

[2] Y. H. Qian, D. d'Humières, and P. Lallemand, "Lattice BGK models for Navier–Stokes equation," *Europhysics Letters*, vol. 17, no. 6, pp. 479–484, 1992.

[3] Q. Zou and X. He, "On pressure and velocity boundary conditions for the lattice Boltzmann BGK model," *Physics of Fluids*, vol. 9, no. 6, pp. 1591–1598, 1997.

[4] U. Ghia, K. N. Ghia, and C. T. Shin, "High-Re solutions for incompressible flow using the Navier–Stokes equations and a multigrid method," *Journal of Computational Physics*, vol. 48, no. 3, pp. 387–411, 1982.